Expanding ASTRA: a unified framework for tokamak and stellarator transport modelling

Plasma Physics and Controlled Fusion

OPEN ACCESS

RECEIVED
14 November 2025

REVISED
10 February 2026

ACCEPTED FOR PUBLICATION
24 March 2026

PUBLISHED
8 April 2026

PAPER

Expanding ASTRA: a unified framework for tokamak and stellarator transport modelling

F Solfronk[1,*], E Fable[1], E Buglione-Ceresa[1], G Tardini[1], M Zanini[2], S Kwak[2], H Zohm[1] and the W7-X Team[3]

[1] Max-Planck-Institut für Plasmaphysik, 85748 Garching, Germany
[2] Max-Planck-Institut für Plasmaphysik, 17491 Greifswald, Germany
[3] See Grulke *et al* 2024 (https://doi.org/10.1088/1741-4326/ad2f4d) for the W7-X Team.
[*] Author to whom any correspondence should be addressed.

E-mail: fabian.solfronk@ipp.mpg.de

Keywords: stellarator, transport modelling, ASTRA, current diffusion equation, flight simulator

Abstract

We present recent developments to the one-dimensional transport solver ASTRA, which will enable the simulation of plasma evolution in both tokamaks and stellarators. To achieve this, a generic current diffusion equation for the poloidal magnetic flux is derived and implemented, together with a coupling to the VMEC equilibrium code. The model is benchmarked against theoretical expectations and validated using experimental data from Wendelstein 7-X, demonstrating that ASTRA can accurately reproduce the evolution of the toroidal current and qualitatively reproduce the occurrence of sawtooth-like instabilities resulting from the rotational transform profile crossing resonant surfaces. With these advancements, ASTRA provides a unified tool for transport studies across different magnetic confinement concepts.

1. Introduction

In the coming years, significant advances are anticipated for both tokamaks and stellarators in the pursuit of operational fusion reactors. To ensure rapid progress, accurate and reliable predictions of plasma evolution within these reactors are essential. High-fidelity integrated modelling suites such as JINTRAC [1] and TOPICS [2] provide detailed, multi-physics, time-dependent simulations for interpretive and predictive studies, but are typically associated with comparatively long run times. Fenix [3–6], a so-called flight simulator, complements these tools by achieving run times of a few minutes through the use of fast, reduced models. It includes the equilibrium solver FEQIS [7] and the plasma transport solver ASTRA [8–10] (the latest version, ASTRA8, is described in [10]) for plasma transport and equilibrium calculations, together with a simulated control system based on the framework of the plasma control system simulation platform [11]. This combination enables comprehensive simulations of plasma scenarios by explicitly capturing interactions between the reactor control system and the plasma [12, 13].

However, both the transport solver ASTRA and the equilibrium solver FEQIS are currently limited to tokamak configurations. The transport equations implemented in ASTRA are, in part, specifically adapted to axisymmetric systems and are therefore not directly applicable to stellarators. In principle, transport solvers for stellarators, such as NTSS [14], do exist, however, these are typically tailored exclusively to stellarator configurations, and solvers expressly designed to simulate both device types are presently lacking. Other codes, such as THRIFT [15–17], evolve only the current diffusion equation for stellarators, but lack the capability to solve energy and particle transport equations. The availability of a single transport solver capable of simulating both tokamaks and stellarators could substantially simplify comparative studies between these two device types. Moreover, extending ASTRA would pave the way for a flight simulator capable of simulating both stellarators and tokamaks.

This work seeks to extend ASTRA's transport modelling capabilities to stellarator configurations. The primary objective is to identify and modify the key transport equations that depend on axisymmetry, while preserving ASTRA's modular framework and expanding its applicability to more general geometries.

The structure of the paper is as follows. In section 2, we review the underlying transport equations used in ASTRA and discuss the modifications required for compatibility with stellarators, including the derivation of a generic current diffusion equation. Section 3 presents a unidirectional coupling between ASTRA and the three-dimensional (3D) equilibrium solver VMEC [18]. In section 4, we validate the generic current diffusion equation: first, by analysing simplified test cases to examine the qualitative evolution of the poloidal magnetic flux, and subsequently by comparison with experimental data from Wendelstein 7-X (W7-X). The final section concludes the paper with a summary of the results and their implications for future research.

2. Upgrading ASTRA's current diffusion equation

2.1. ASTRA transport equations

In [19], a set of transport equations is derived under the assumptions of axisymmetry, the existence of nested magnetic flux surfaces, flux-surface averaging with fast parallel equilibration, and a fluid description of the plasma species based on distribution functions close to Maxwellian. Based on the work presented in [19], the main transport equations solved in ASTRA are given in [8]:

$$\frac{1}{V'}\left(\frac{\partial}{\partial t}-\frac{\dot{B}_0}{2B_0}\frac{\partial}{\partial \rho}\rho\right)\left(V' n_\mathrm{s}\right)=-\frac{1}{V'}\frac{\partial}{\partial \rho}\Gamma_\mathrm{s}+S_\mathrm{s} \tag{1}$$

$$\frac{3}{2}\left(V'\right)^{-\frac{5}{3}}\left(\frac{\partial}{\partial t}-\frac{\dot{B}_0}{2B_0}\frac{\partial}{\partial \rho}\rho\right)\left(\left(V'\right)^{\frac{5}{3}} n_\mathrm{s} T_\mathrm{s}\right)=-\frac{1}{V'}\frac{\partial}{\partial \rho}q_\mathrm{s}+P_\mathrm{s} \tag{2}$$

$$\sigma_{\parallel}\left(\frac{\partial \Psi}{\partial t}-\frac{\rho \dot{B}_0}{2B_0}\frac{\partial \Psi}{\partial \rho}\right)=\frac{J^2 R_0}{\mu_0 \rho}\frac{\partial}{\partial \rho}\left(\frac{G_2}{J}\frac{\partial \Psi}{\partial \rho}\right)-\frac{V'}{2\pi\rho}\left(j_\mathrm{BS}+j_\mathrm{CD}\right) \tag{3}$$

where n_s and T_s denote the density and temperature of particle species s, Ψ is the poloidal magnetic flux, Γ_s and q_s represent the particle and energy fluxes, and S_s and P_s are the particle and energy sources, respectively. j_BS and j_CD denote the bootstrap and externally driven currents; R_0 and B_0 are reference major radius and vacuum magnetic field at the reference major radius. $\sigma_{\parallel}$ denotes the parallel conductivity, and μ_0 the vacuum permeability. Furthermore, ρ is defined as $(\Phi/(\pi B_0))^{0.5}$, where Φ is the toroidal magnetic flux. The radial derivative of the volume, V', is defined as $\partial V/\partial\rho$. The geometrical parameter G_2 is given by $V'/(4\pi^2)\left\langle(\nabla\rho/R)^2\right\rangle$, where the notation $\langle f\rangle$ indicates the flux surface average of a quantity f. As shown in [8], the normalised poloidal current J can be expressed as $4\pi^2\rho R_0/V'\left\langle(R_0/R)^2\right\rangle^{-1}$.

Equations (1) and (2) are already generic, and, as shown in [19], can be derived without assuming axisymmetry. The time-derivative operator on the left-hand side of equations (1) and (2) includes an advective derivative term, the second term (in the case of equation (1): $\partial_\rho(\partial_t\rho|_\Phi\, V' n_\mathrm{s}) = -\dot{B}_0/(2B_0)\partial_\rho(\rho V' n_\mathrm{s})$), which accounts for changes in n_s and $n_\mathrm{s}T_\mathrm{s}$ arising from variations of the radial coordinate ρ at constant Φ. Consequently, the explicit form of this term depends on the particular definition of ρ, which is in general not uniquely specified. Thus, the appearance of B_0 and its time derivative arises solely from the definition of the radial coordinate ρ, and not from assuming axisymmetry. In the context of stellarators, B_0 is defined as the average magnetic field on axis. Nevertheless, it is important to emphasise that the explicit forms of individual terms in these equations may still depend on the underlying geometry. For example, neoclassical transport coefficients differ between tokamaks and stellarators [20–22]. In this work, the individual transport and bootstrap coefficients are treated as input parameters for ASTRA, to be supplied by the user conducting the simulation.

The treatment of current diffusion is more complex. In the remainder of this section, a generic equation governing the evolution of the poloidal magnetic flux is derived. It is further shown that equation (3) represents only a special case of the generic current diffusion equation, obtained under the assumption of axisymmetric geometry.

2.2. Generic current diffusion equation

In [15], a generic equation describing the evolution of the rotational transform, $\iota = \hat{\Psi}'/\hat{\Phi}'$, was derived under the assumption that a set of nested flux surfaces exists. $\hat{\Psi}$ and $\hat{\Phi}$ denote poloidal and toroidal

magnetic flux as defined in [15]:

$$\hat{\Psi}(\rho) \equiv \int_0^{2\pi} \mathrm{d}\zeta \int_0^{\rho} \sqrt{g} B^{\theta} \mathrm{d}\tilde{\rho} \tag{4}$$

$$\hat{\Phi}(\rho) \equiv \int_0^{2\pi} \mathrm{d}\theta \int_0^{\rho} \sqrt{g} B^{\zeta} \mathrm{d}\tilde{\rho}. \tag{5}$$

The curvilinear coordinate system is defined by the flux surface label ρ, the poloidal angle θ, and the toroidal angle ζ. It should be noted that the formulation of equations (4) and (5) does not further constrain ρ, other than designating it as a label for the flux surfaces. $\tilde{\rho}$ is used as the integration variable to distinguish it from the upper limit ρ. The quantity $\sqrt{g}$ denotes the Jacobian of the transformation from the curvilinear to Cartesian coordinates. B^{θ} and B^{ζ} represent the contravariant poloidal and toroidal components of the magnetic field, respectively. The current diffusion equation from [15] is rewritten here for the sake of compactness:

$$\left.\frac{\partial \iota}{\partial t}\right|_{\rho} = \frac{\partial \iota}{\partial \hat{\Phi}} \left.\frac{\partial \hat{\Phi}}{\partial t}\right|_{\rho} + \frac{\partial}{\partial \hat{\Phi}} \left\{ \frac{1}{\sigma_{\parallel} \mu_0} \hat{\Phi}' \left(S_{21}\iota + S_{22}\right)^2 \frac{\partial}{\partial \rho} \left[\frac{S_{11}\iota + S_{12}}{S_{21}\iota + S_{22}}\right] - \frac{B_0}{\sigma_{\parallel}} \left(j_{\mathrm{BS}} + j_{\mathrm{CD}}\right) \frac{\partial V}{\partial \hat{\Phi}} \right\} \tag{6}$$

where the definitions of the bootstrap and externally driven current densities, as used in ASTRA, have been applied: $j_{\mathrm{BS}} \equiv \langle \vec{J}_{\mathrm{BS}} \cdot \vec{B} \rangle / B_0$ and $j_{\mathrm{CD}} \equiv \langle \vec{J}_{\mathrm{CD}} \cdot \vec{B} \rangle / B_0$. Here, $\left.\partial f / \partial t\right|_{\rho}$ represents the time derivative of a quantity f, taken at fixed ρ. The elements of the susceptance matrix S_{ij} are defined in [15] as

$$\mu_0 \begin{pmatrix} I \\ F \end{pmatrix} = \begin{pmatrix} S_{11} & S_{12} \\ S_{21} & S_{22} \end{pmatrix} \begin{pmatrix} \hat{\Psi}' \\ \hat{\Phi}' \end{pmatrix} \tag{7}$$

where I and F are toroidal and poloidal currents as defined in [15]. This relation yields an equation for the rotational transform ι:

$$\iota = \frac{\hat{\Psi}'}{\hat{\Phi}'} = \frac{\mu_0 I}{S_{11} \hat{\Phi}'} - \frac{S_{12}}{S_{11}}. \tag{8}$$

Hence, the vacuum rotational transform is given by $\iota_{\mathrm{vac}} = -S_{12}/S_{11}$. As demonstrated in [23], the susceptance matrix is diagonal in the axisymmetric case, showing that $\iota_{\mathrm{vac}} = 0$ for a tokamak.

Integrating equation (6) over $\hat{\Phi}$ yields

$$\left.\frac{\partial \hat{\Psi}}{\partial t}\right|_{\rho} + U_{\zeta,\mathrm{l,axis}} = \iota \left.\frac{\partial \hat{\Phi}}{\partial t}\right|_{\rho} + \frac{1}{\sigma_{\parallel} \mu_0} \hat{\Phi}' \left(S_{21}\iota + S_{22}\right)^2 \frac{\partial}{\partial \rho} \left[\frac{S_{11}\iota + S_{12}}{S_{21}\iota + S_{22}}\right] - \frac{B_0}{\sigma_{\parallel}} \left(j_{\mathrm{BS}} + j_{\mathrm{CD}}\right) \frac{\partial V}{\partial \hat{\Phi}}. \tag{9}$$

As shown in [15], the corresponding integration constant can be identified as the axial toroidal loop voltage, $U_{\zeta,\mathrm{l,axis}}$, defined as $\int_0^{2\pi} E_{\zeta}(\rho = 0) \mathrm{d}\zeta$. E_{ζ} denotes the covariant toroidal component of the electric field.

In ASTRA, the poloidal magnetic flux is defined as the flux through the surface spanning from the central axis (the z-axis in a Cartesian coordinate system) to the corresponding flux surface labelled by ρ:

$$\Psi(\rho) \equiv -\int_0^{2\pi} \mathrm{d}\zeta \int_{\rho}^{\infty} \sqrt{g} B^{\theta} \mathrm{d}\tilde{\rho} = \hat{\Psi}(\rho) + \Psi(0). \tag{10}$$

The toroidal flux Φ is defined as in [15]: $\Phi = \hat{\Phi}$. As $\Psi_0 \equiv \Psi(0)$, the flux through the poloidal surface spanning from the central axis to the magnetic axis, does not exhibit any radial dependence, the radial derivatives of the magnetic fluxes are identical for both definitions: $\Psi' = \hat{\Psi}'$ and $\Phi' = \hat{\Phi}'$. Consequently, the definition of the susceptance matrix remains unchanged if the ASTRA fluxes are employed in equation (7). The same holds for the rotational transform, which also depends solely on the radial derivatives of the fluxes (cf equation (8)). By applying Faraday's law of induction and Stokes' theorem, the temporal derivative of Ψ_0 can be identified as

$$\frac{\partial \Psi_0}{\partial t} = -\frac{\partial}{\partial t} \left(\int_0^{2\pi} \mathrm{d}\zeta \int_0^{\infty} \sqrt{g} B^{\theta} \mathrm{d}\rho \right) = \int_0^{2\pi} E_{\zeta}(\rho = 0) \, \mathrm{d}\zeta = U_{\zeta,\mathrm{l,axis}}. \tag{11}$$

Rewriting equation (9) in terms of Ψ and Φ yields

$$\left.\frac{\partial \Psi}{\partial t}\right|_{\rho} = \iota \left.\frac{\partial \Phi}{\partial t}\right|_{\rho} + \frac{1}{\sigma_{\parallel} \mu_0} \Phi' \left(S_{21}\iota + S_{22}\right)^2 \frac{\partial}{\partial \rho} \left[\frac{S_{11}\iota + S_{12}}{S_{21}\iota + S_{22}}\right] - \frac{B_0}{\sigma_{\parallel}} \left(j_{\mathrm{BS}} + j_{\mathrm{CD}}\right) \frac{\partial V}{\partial \Phi}. \tag{12}$$

Using the ASTRA definition of ρ ($\Phi = \rho^2 B_0 \pi$), equation (12) can be rewritten in terms of a single radial coordinate, ρ. By rearranging equation (12), one obtains

$$\sigma_{\parallel} \left(\frac{\partial \Psi}{\partial t} - \frac{\rho \dot{B}_0}{2B_0} \frac{\partial \Psi}{\partial \rho} \right) = \frac{2\pi B_0 \rho}{\mu_0} \left(S_{21} \iota + S_{22} \right)^2 \cdot \frac{\partial}{\partial \rho} \left[\frac{1}{S_{21}\iota + S_{22}} \left(\frac{S_{11}}{2\pi B_0 \rho} \frac{\partial \Psi}{\partial \rho} + S_{12} \right) \right] - \frac{V'}{2\pi \rho} \left(j_{\mathrm{BS}} + j_{\mathrm{CD}} \right). \tag{13}$$

As in the original transport equations of ASTRA (equations (1)–(3)), the time derivative operator on the left hand side of equation (13) includes an advective derivative operator (second term), which accounts for changes in Ψ that arise from variations of the radial coordinate ρ at constant Φ. Its explicit form depends on the particular definition of the radial coordinate ρ, which is in general not uniquely specified. In the context of stellarators, B_0 denotes the average magnetic field on axis. For most stellarator discharge scenarios, the temporal derivative $\dot{B}_0$ is small due to the stability of the equilibrium, allowing the corresponding term in equation (13) to be neglected.

In ASTRA, the transport equations are solved semi-implicitly to ensure fast runtimes but accurate and stable evolution of the profiles. For example, radial derivatives of temperature and density from the previous time step are used to compute the particle and heat fluxes required to solve the transport equations (1) and (2). The remaining rotational transforms in equation (13), which are functions of the poloidal magnetic flux ($\iota = \partial\Psi/\partial\Phi \sim \rho^{-1}\partial\Psi/\partial\rho$), are treated in a similar fashion. Specifically, when solving the newly implemented generic current diffusion equation, these terms are approximated using the solution from the previous time step. Consequently, $\iota_t \approx \iota_{t-\tau}$ is used for the two remaining occurrences of ι in equation (13), under the assumption that changes in ι over a single time step τ (typically on the order of a few ms) are sufficiently small. With this modification, equation (13) adopts a structure analogous to that of equations (1)–(3), and can therefore be solved in a similar manner.

Regarding the boundary condition for the current diffusion equation, an external circuit equation is solved:

$$U_{\mathrm{ext}} = U_{\mathrm{pl}} \left(\rho_{\mathrm{B}} \right) + \frac{\mathrm{d}}{\mathrm{d}t} \left(L_{\mathrm{ext}} I_{\mathrm{tor}} \right) \tag{14}$$

where U_{ext} is the voltage produced by the external current-carrying conductors, which has to be provided for each timestep. For stellarators, U_{ext} can be set to zero. $U_{\mathrm{pl}}(\rho_{\mathrm{B}}) = \partial\Psi/\partial t|\,\rho_{\mathrm{B}}$ denotes the loop voltage at the separatrix ($\rho = \rho_{\mathrm{B}}$), L_{ext} is the external inductance of the plasma column, and I_{tor} is the toroidal current within the last closed flux surface (LCFS). In this work, the value of L_{ext} was calculated based on the results presented in [24] for the axisymmetric case. Evidently, this provides only an approximation for stellarators. However, while L_{ext} may in detail differ from that of a tokamak, it is expected that the difference is not substantial [24, 25]. In practice, this approach has proven sufficiently accurate for the cases considered in this study. Nevertheless, a proper treatment of the external coupling between the plasma and the coils, accounting for 3D geometry, will be pursued in the future. For the calculation of L_{ext}, an elongation of 1.0 was assumed for the W7-X geometry. The total toroidal current I_{tor} can be calculated using equation (8), together with the definition of ρ:

$$I_{\mathrm{tor}} = \frac{S_{11}\left(\rho_{\mathrm{B}}\right)}{\mu_0} \left(\left. \frac{\partial \Psi}{\partial \rho} \right|_{\rho_{\mathrm{B}}} - 2\pi B_0 \rho_{\mathrm{B}} \iota_{\mathrm{vac}} \left(\rho_{\mathrm{B}} \right) \right). \tag{15}$$

Substituting equations (15) into (14) and integrating over time yields a Robin boundary condition for the current diffusion equation:

$$\Psi \left(\rho_{\mathrm{B}} \right) + L_{\mathrm{ext}} \frac{S_{11}\left(\rho_{\mathrm{B}}\right)}{\mu_0} \left. \frac{\partial \Psi}{\partial \rho} \right|_{\rho_{\mathrm{B}}} = \Psi_{\mathrm{ext}} + \frac{2\pi B_0 \rho_{\mathrm{B}}}{\mu_0} L_{\mathrm{ext}} S_{11} \left(\rho_{\mathrm{B}} \right) \iota_{\mathrm{vac}} \left(\rho_{\mathrm{B}} \right) \tag{16}$$

where Ψ_{ext} is defined as $\int_{t-\tau}^{t} U_{\mathrm{ext}}\,\mathrm{d}t'$.

For comparison with experimental data, the poloidal magnetic flux is usually of less interest than, for example, the total toroidal current, the current density, and the rotational transform. After solving equation (13) to obtain the poloidal magnetic flux, the rotational transform is calculated using $\iota = \Psi'/\Phi'$. The total toroidal current, I_{tor}, can be computed using equation (15), and the parallel current density $j_{\parallel}$ is calculated as follows:

$$j_{\parallel} \equiv \frac{\langle \vec{J} \cdot \vec{B} \rangle}{B_0} = \frac{\mu_0}{V' B_0} \left(F I' - I F' \right) = \frac{\mu_0}{V' B_0} F^2 \frac{\partial}{\partial \rho} \left(\frac{I}{F} \right). \tag{17}$$

Equation (11) from [15] was employed to derive this formula. The currents F and I can be calculated using equation (7).

2.3. Consistency with the axisymmetric case

The following subsection is devoted to demonstrating that the originally implemented equation for the evolution of the poloidal magnetic flux (equation (3)) is a special case of the generic current diffusion equation (13), obtained under the assumption of axisymmetric magnetic geometry.

As previously mentioned, in the axisymmetric case the susceptance matrix is diagonal. Accordingly, equation (13) reduces to

$$\sigma_{\parallel}\left(\frac{\partial\Psi}{\partial t}-\frac{\rho\dot{B}_0}{2B_0}\frac{\partial\Psi}{\partial\rho}\right)=\frac{S_{22}^2\rho}{\mu_0}\frac{\partial}{\partial\rho}\left(\frac{S_{11}}{S_{22}\rho}\frac{\partial\Psi}{\partial\rho}\right)-\frac{V'}{2\pi\rho}\left(j_{\mathrm{BS}}+j_{\mathrm{CD}}\right). \tag{18}$$

In [15], the diagonal elements of the susceptance matrix were derived for the axisymmetric case:

$$S_{11}=\frac{V'}{4\pi^2}\left\langle\left(\frac{\nabla\rho}{R}\right)^2\right\rangle \tag{19}$$

$$S_{22}=\frac{4\pi^2}{V'}\frac{1}{\langle R^{-2}\rangle}. \tag{20}$$

Thus, they can be expressed in terms of the geometric parameter G_2 and the normalised poloidal current J from equation (3):

$$S_{11}=G_2 \tag{21}$$

$$S_{22}=\frac{R_0 J}{\rho}. \tag{22}$$

Consequently, the first term on the right-hand side of equation (18) can be represented by J and G_2:

$$\frac{S_{22}^2\rho}{\mu_0}\frac{\partial}{\partial\rho}\left(\frac{S_{11}}{S_{22}\rho}\frac{\partial\Psi}{\partial\rho}\right)=\frac{J^2R_0}{\mu_0\rho}\frac{\partial}{\partial\rho}\left(\frac{G_2}{J}\frac{\partial\Psi}{\partial\rho}\right). \tag{23}$$

Substituting the right-hand side of equation (23) into equation (18) demonstrates that the newly implemented generic current diffusion equation (13) indeed reduces to the original equation in ASTRA (equation (3)) under the assumption of axisymmetric magnetic geometry.

As a so-called 1.5D transport solver, ASTRA is coupled to the 2D equilibrium solver FEQIS. However, FEQIS is not capable of calculating 3D stellarator equilibria. Therefore, an alternative equilibrium solver must be coupled to ASTRA. For this purpose, VMEC [18] has been chosen. The technical details of this coupling are described in the next section.

3. Coupling of VMEC to ASTRA

At present, only a unidirectional coupling between VMEC and ASTRA exists; that is, ASTRA reads equilibria calculated by VMEC, but does not generate an input file for VMEC in return. A bidirectional coupling is planned for the future, however, for fast applications of ASTRA, the runtime of VMEC when handling 3D stellarator geometry remains too long. Nevertheless, as stellarator equilibria are comparatively stable over the course of an experimental discharge, robust results can already be achieved by using a precomputed, for instance, experimental, equilibrium and assuming it remains constant throughout the simulation. For discharge scenarios with large variations of the plasma β, which can significantly affect the magnetic geometry [20], the bidirectional coupling will likely be necessary. In the following, the unidirectional coupling of VMEC to ASTRA is described.

For the particular choice of a coordinate system (ρ,θ,ζ), where ρ denotes the radial coordinate, θ the poloidal angle, and ζ the toroidal angle, the magnetic field $\vec{B}$ can be expressed as [18]

$$\vec{B}=\frac{1}{2\pi}\left(\nabla\zeta\times\nabla\Psi+\nabla\Phi\times\nabla\theta^*\right) \tag{24}$$

where θ^* is defined as

$$\theta^*=\theta+\lambda(\rho,\theta,\zeta) \tag{25}$$

and λ is a periodic function in θ and ζ, which straightens the field lines [18]. As demonstrated in [26], in such a coordinate system the elements of the susceptance matrix can be expressed as

$$S_{11} = \frac{V'}{4\pi^2}\left\langle \frac{g_{\theta\theta}}{g} \right\rangle \tag{26}$$

$$S_{12} = \frac{V'}{4\pi^2}\left\langle \frac{g_{\theta\zeta}\,(1+\lambda_{,\theta}) - g_{\theta\theta}\lambda_{,\zeta}}{g} \right\rangle \tag{27}$$

$$S_{21} = \frac{V'}{4\pi^2}\left\langle \frac{g_{\zeta\theta}}{g} \right\rangle \tag{28}$$

$$S_{22} = \frac{V'}{4\pi^2}\left\langle \frac{g_{\zeta\zeta}\,(1+\lambda_{,\theta}) - g_{\zeta\theta}\lambda_{,\zeta}}{g} \right\rangle \tag{29}$$

where $\lambda_{,\alpha}$ is defined as $\partial\lambda/\partial\alpha$, g is the squared Jacobian of the transformation from the curvilinear to Cartesian coordinates, $g_{\alpha\beta}$ is an element of the metric tensor, and $V' = \partial V/\partial\rho$ denotes the radial derivative of volume, as defined in the previous section.

In VMEC, the computed equilibrium provides the major radius R and the vertical position z as functions of ρ, θ and ζ, where ζ is identified with the toroidal coordinate ϕ in a cylindrical coordinate system. These functions can be used to calculate the elements $g_{\alpha\beta}$ of the metric tensor, which are defined by $\partial\vec{x}/\partial\alpha \cdot \partial\vec{x}/\partial\beta$:

$$g_{\theta\theta} = \left(\frac{\partial R}{\partial\theta}\right)^2 + \left(\frac{\partial z}{\partial\theta}\right)^2 \tag{30}$$

$$g_{\zeta\zeta} = \left(\frac{\partial R}{\partial\zeta}\right)^2 + \left(\frac{\partial z}{\partial\zeta}\right)^2 + R^2 \tag{31}$$

$$g_{\theta\zeta} = g_{\zeta\theta} = \frac{\partial R}{\partial\theta}\frac{\partial R}{\partial\zeta} + \frac{\partial z}{\partial\theta}\frac{\partial z}{\partial\zeta}. \tag{32}$$

Moreover, geometrical quantities such as the radial derivative of the volume, V', as well as the specific form of $\lambda(\rho,\theta,\zeta)$, are provided. Thus, all necessary ingredients for calculating the susceptance matrix according to equations (26)–(29) are supplied by VMEC.

For the coupling with ASTRA, a Python routine was developed to compute all required geometric quantities based on a *wout* file (i.e. output file) generated by VMEC, and to interpolate them onto the ASTRA grid. To process the output file and compute the susceptance matrix, the VMEC class from the pySTEL software is utilised. PySTEL itself employs the Fortran-based LIBSTELL library to read the *wout* file. Both are part of the STELLOPT GitHub repository [27].

As shown in the equations (26)–(29), the susceptance matrix depends on the metric tensor and, consequently, on the underlying coordinate system. Therefore, before applying the susceptance matrix in ASTRA, the elements must be transformed from the VMEC coordinate system to that used in ASTRA. While in VMEC $\zeta = \phi$ is used, ASTRA's toroidal angle points into the opposite direction, i.e. $\zeta = -\phi$. Additionally, the radial coordinate in VMEC is defined as $s_{\mathrm{VMEC}} = \Phi/\Phi_{\mathrm{sep}}$, whereas in ASTRA it is $\rho_{\mathrm{ASTRA}} = (\Phi/(\pi B_0))^{0.5}$.

The impact on the metric tensor components can be deduced from equations (30)–(32). Reversing the direction of ζ only changes the signs of $g_{\theta\zeta}$ and $g_{\zeta\theta}$, while the remaining metric tensor elements remain unaffected. The redefinition of the radial coordinate does not alter the metric tensor components presented here. Similarly, only $\lambda_{,\zeta}$ is affected by the change in coordinate system (its sign is reversed), whereas $\lambda_{,\theta}$ remains unchanged. To calculate the Jacobian, $(\sqrt{g})_{\mathrm{ASTRA}}$, the metric tensor must be transformed to the ASTRA coordinate system via $\mathbf{g}_{\mathrm{ASTRA}} = \mathbf{J}^T\mathbf{g}_{\mathrm{VMEC}}\mathbf{J}$, where

$$\mathbf{J} = \mathrm{diag}\left(\frac{\partial s_{\mathrm{VMEC}}}{\partial\rho_{\mathrm{ASTRA}}} = \frac{2\pi B_0}{\Phi_{\mathrm{sep}}}\rho_{\mathrm{ASTRA}}, 1, \frac{\partial\phi}{\partial(-\phi)} = -1\right) \tag{33}$$

is the Jacobian matrix from the VMEC to the ASTRA coordinate system. Consequently,

$$\begin{aligned}(\sqrt{g})_{\mathrm{ASTRA}} &= \sqrt{\det\mathbf{g}_{\mathrm{ASTRA}}} = |\det\mathbf{J}|\sqrt{\det\mathbf{g}_{\mathrm{VMEC}}} \\ &= \frac{2\pi B_0}{\Phi_{\mathrm{sep}}}\rho_{\mathrm{ASTRA}}\,(\sqrt{g})_{\mathrm{VMEC}}.\end{aligned} \tag{34}$$

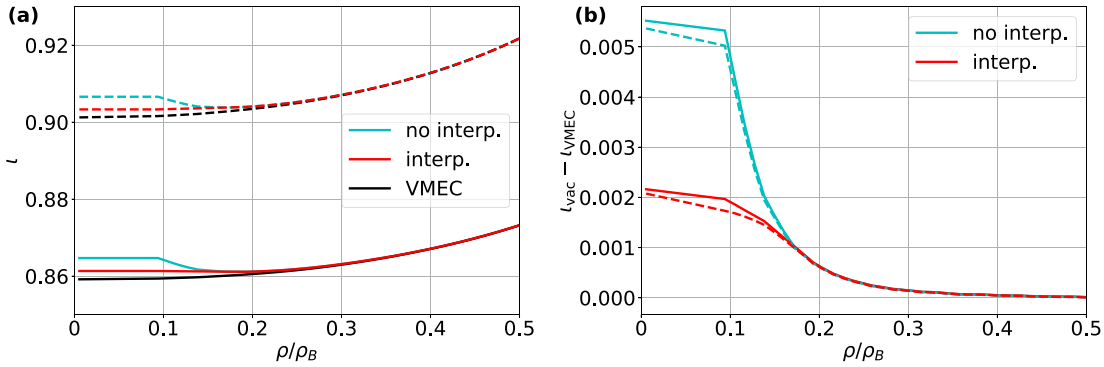

Figure 1. (a) Comparison between the rotational transform provided by VMEC (black) and $\iota_{\mathrm{vac}} = -S_{12}/S_{11}$ computed for ASTRA (red and cyan) for W7-X discharges 20230216.059 (dashed lines) and 20171206.025 (solid line). The red curves show ι_{vac} with quadratic interpolation applied to the second and third element of S_{11} and S_{12}, while the cyan curves correspond to profiles without interpolation in the core. (b): Deviation of the computed ι_{vac} from the VMEC rotational transform.

Since the flux surface integral, calculated for S_{ij}, is proportional to $(\sqrt{g})^{-1}$, the susceptance matrix transformed into the ASTRA coordinate system is given by

$$S_{ij,\mathrm{ASTRA}} = \left(2\delta_{ij} - 1\right) \frac{\Phi_{\mathrm{sep}}}{2\pi B_0 \rho_{\mathrm{ASTRA}}} S_{ij,\mathrm{VMEC}} \tag{35}$$

where δ_{ij} denotes the Kronecker delta symbol. The δ_{ij} term accounts for the sign changes of $g_{\theta\zeta}$, $g_{\zeta\theta}$, and $\lambda_{,\zeta}$. It should be noted that the reversal of the ζ coordinate not only affects the susceptance matrix, but also other quantities provided by VMEC. For instance, the sign of the axial magnetic field B_0 and the toroidal magnetic flux Φ is also reversed.

During this study, it became apparent that numerical issues arise rapidly when calculating $\iota_{\mathrm{vac}} = -S_{12}/S_{11}$ in the plasma core. This is due to $S_{12}(0) = S_{11}(0) = 0$, which in turn arises because $\partial R/\partial\theta$ and $\partial z/\partial\theta$ vanish at $\rho = 0$. The extent of these numerical issues is illustrated in figure 1.

In the previously mentioned Python script, the susceptance matrix is calculated using pySTEL, transformed to the ASTRA coordinate system via equation (35), linearly interpolated from the VMEC grid to the ASTRA grid, and ι_{vac} is then computed on the ASTRA grid from the resulting susceptance matrix elements. The resulting ι_{vac} for the W7-X discharges 20230216.059 (dashed lines) and 20171206.025 (solid line) is shown in figure 1(a) (in cyan), and compared with the ι profile obtained from the corresponding vacuum reference equilibria supplied by VMEC (black). As these equilibria contained no toroidal current, the ι profile from VMEC corresponds to the vacuum rotational transform of each equilibrium. However, for $\rho_{\mathrm{ASTRA}}/\rho_{\mathrm{B}} \lesssim 0.2$, the computed ι_{vac} differs from the VMEC rotational transform, as illustrated in figure 1(b), which shows the deviation of the calculated ι_{vac} from ι_{VMEC}.

To avoid such deviations in the core, the values of S_{11}, S_{12}, and S_{21}, once transformed into the ASTRA coordinate system using equation (35), were quadratically interpolated at the second and third innermost radial VMEC grid points ($\rho_{\mathrm{ASTRA}}/\rho_{\mathrm{B}} \approx 0.10$ and $\rho_{\mathrm{ASTRA}}/\rho_{\mathrm{B}} \approx 0.14$), with the constraint $S_{11}(0) = S_{12}(0) = S_{21}(0) = 0$. The choice to interpolate at the second and third innermost grid points was a compromise between limiting the extent of the interpolation and achieving the best possible correction to the ι_{vac} profile. The applied VMEC equilibria contained 91 radial grid points. In the case of VMEC equilibria with more radial grid points, it may be necessary to interpolate at more than just the second and third innermost points. In figure 1, ι_{vac} and its deviation from ι_{VMEC}, including the effect of quadratic interpolation in the core, are illustrated in red. For both equilibria, a reduction in the numerical error is evident.

It should be noted that, in the simulations presented in section 4.2, the difference between interpolating and not interpolating S_{11}, S_{12}, and S_{21} in the plasma core was negligible. This is primarily because the difference in the core between the VMEC vacuum rotational transform and the value calculated without interpolation remains very small, approximately 0.005 (see figure 1(b)). However, this may not be the case for all equilibria, which is why this point is emphasised here. In the absence of interpolation, larger deviations may cause instabilities associated with resonant surfaces to be triggered earlier or later in the simulation than in the experiment, thereby altering the discharge evolution.

Figures 2(a)–(c) show the computed susceptance matrix elements S_{11}, S_{12}, and S_{21} in the ASTRA coordinate system and on the ASTRA radial grid for the vacuum reference equilibrium of discharge 20171206.025. The susceptance matrix elements obtained without interpolation in the core are also

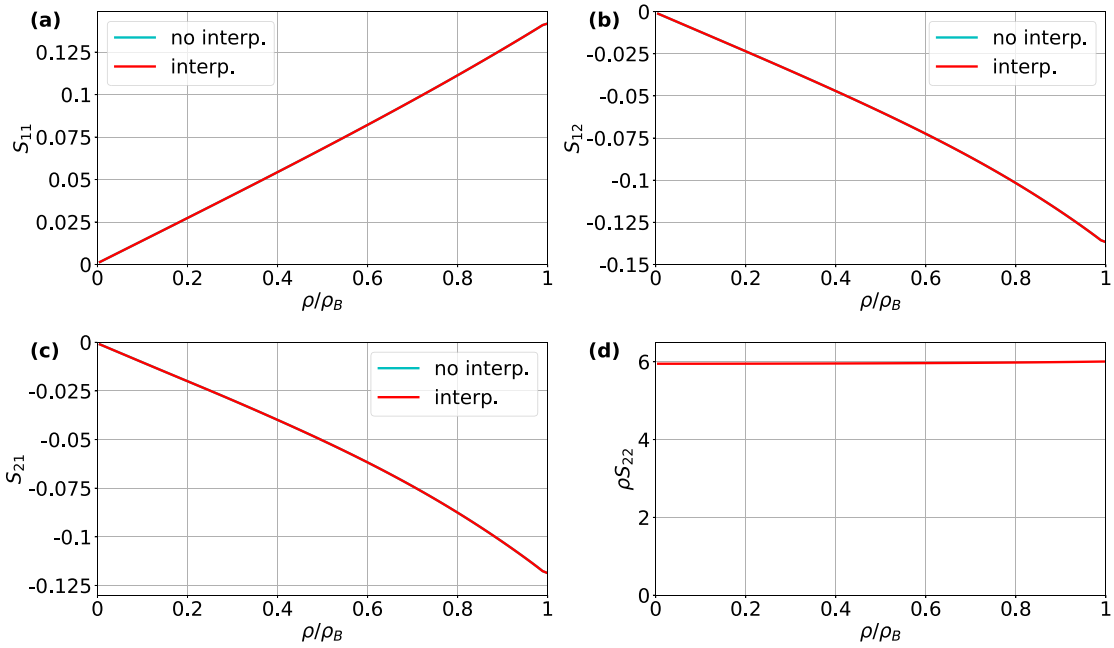

Figure 2. Susceptance matrix elements (in the ASTRA coordinate system and on the ASTRA radial grid) for the vacuum reference equilibrium of W7-X discharge 20171206.025. In (a)–(c), both the profiles with and without quadratic interpolation in the core are shown. As the profiles overlap closely, the difference is not visible. The profile without quadratic interpolation in the core lies behind the one with interpolation.

shown, however, they are not visible, as they are overlaid by the elements with interpolation. This illustrates that the quadratic interpolation in the core has only a minor effect on the susceptance matrix elements themselves, whereas its impact on ι_{vac}, and consequently on ι, can be substantial, as illustrated in figure 1. As S_{22} does not, in general, vanish in the core, but $S_{22,\mathrm{ASTRA}} \sim S_{22,\mathrm{VMEC}}/\rho_{\mathrm{ASTRA}}$, $S_{22,\mathrm{ASTRA}}$ diverges as ρ_{ASTRA} approaches zero. To avoid numerical instabilities, the variable $\rho_{\mathrm{ASTRA}} S_{22,\mathrm{ASTRA}}$ was implemented in ASTRA, rather than $S_{22,\mathrm{ASTRA}}$ itself. As can be seen in figure 2(d), $\rho_{\mathrm{ASTRA}} S_{22,\mathrm{ASTRA}}$ tends to have a small radial gradient, so additional interpolation of $\rho_{\mathrm{ASTRA}} S_{22,\mathrm{ASTRA}}$ in the core, as performed for S_{11}, S_{12} and S_{21}, is not necessary.

In the next section, the generic current diffusion equation is validated, beginning with simple theoretical examples and subsequently including a comparison with experimental measurements from W7-X.

4. Validation

At first, three simple example cases of simulations employing the generic current diffusion equation (13) are presented. These are intended to verify whether solving the equation produces the physically expected evolution of the current density and ι profile. In the second subsection, the current diffusion equation is validated against the evolution of the toroidal current observed in W7-X discharges 20171206.025 and 20171206.036.

Both discharges, 20171206.025 and 20171206.036, share the same vacuum reference equilibrium, which was calculated using VMEC. This equilibrium is employed in the following two subsections to determine the susceptance matrix required for the simulations. For section 4.2, this approach assumes a sufficiently stable equilibrium throughout the simulated time interval. The parallel conductivity, $\sigma_{\parallel}$, was calculated using the formula presented in [28], which does not account for all the effects arising from the 3D geometry inherent in a stellarator configuration [30], and may therefore only be considered an approximation of the actual parallel conductivity. At present, a coupling between ASTRA and the code DKES [31, 32] is under development and will be realised via look-up tables. In future studies, this will enable the provision of neoclassical transport coefficients, the radial electric field, bootstrap current coefficients, and the parallel conductivity in a manner that remains fast but is more accurate than the approach used in this work. The fraction of trapped particles, f_t, required for the computation of the parallel conductivity, was determined from the VMEC equilibrium according to the expression given in [29, 30]. The kinetic profiles used to calculate the conductivity are fixed in section 4.1 and are based

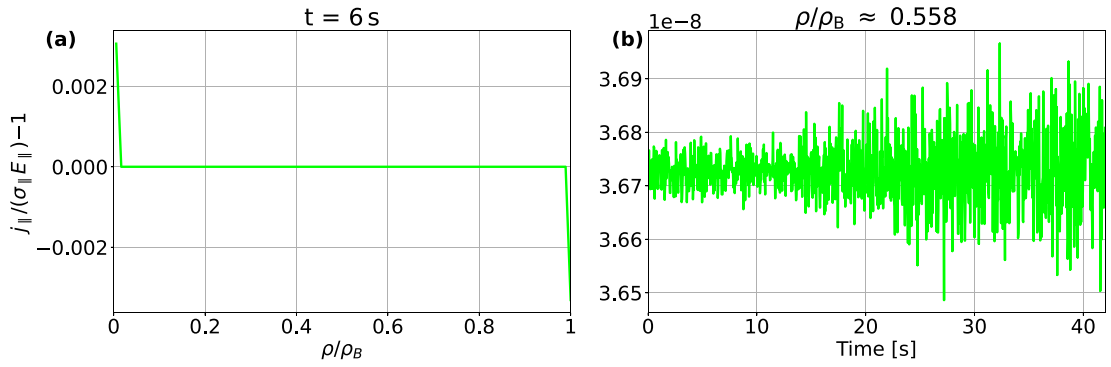

Figure 3. Confirmation of Ohm's law for the tokamak case. (a) Radial verification of Ohm's law at an arbitrarily selected time point (6 s). (b) Temporal verification of Ohm's law at arbitrarily selected radial location ($\rho/\rho_B \approx 0.558$).

on measurements from discharge 20171206.025, using Thomson Scattering [33, 34] and ECE [35] diagnostics, and subsequently fitted with Profile Cooker [36]. In section 4.2, selected time points from the discharges were used to extract kinetic profiles, and ASTRA automatically interpolates between these profiles. Experimental measurements of the bremsstrahlung and Bayesian modelling [37–39] were used to obtain experimental effective charge profiles for the discharges investigated in section 4.2. These profiles were then applied in the simulations presented in section 4.2 to calculate the conductivity.

4.1. Consistency checks with theoretical expectations

The first example case presented in this subsection simulates a plasma current as in a tokamak, in order to verify whether the evolution of the parallel current density still satisfies Ohm's law, $j_\parallel = \sigma_\parallel E_\parallel$. The parallel current density, $j_\parallel$, was calculated using equation (17), while $E_\parallel$ was computed as $E_\parallel = U_\parallel/(2\pi R_0) = 2\pi\rho/V'\,\partial\Psi/\partial t$, with the latter relation shown in [8] for tokamak geometry. To mimic tokamak conditions, the off-axis elements of the susceptance matrix were set to zero, and U_{ext} in equation (14) was set to 0.1 V in order to drive a plasma current. No external current drive was simulated, and the bootstrap current was neglected. The result of this simulation is presented in figure 3. Analytically, $j_\parallel/(\sigma_\parallel E_\parallel) - 1$ is zero according to Ohm's law. As shown in figure 3(a), this is approximately the case across the entire radial profile. At the innermost and outermost grid points, a deviation on the order of 10^{-3} is visible, originating from approximating radial derivatives at the grid boundaries during the calculation of $j_\parallel$. At all other grid points, the numerical error is only on the order of 10^{-8}, as seen in figure 3(b), which shows the temporal evolution of $j_\parallel/(\sigma_\parallel E_\parallel) - 1$ at the randomly chosen radial position $\rho/\rho_B \approx 0.558$. Consequently, Ohm's law is still obeyed by the implemented generic current diffusion equation, both in space (see figure 3(a)) and in time (see figure 3(b)), apart from negligible numerical deviations.

Now, the temporal evolution of $j_\parallel$ and ι will be examined for the stellarator case. In a tokamak, in the absence of non-inductive current drive and of an externally induced loop voltage, the toroidal plasma current decays and, consequently, the poloidal magnetic field generated by the plasma weakens. As a result, the rotational transform ι tends to zero, and plasma confinement collapses. By contrast, in a stellarator the external coils generate both toroidal and poloidal vacuum magnetic fields, which produce nested flux surfaces and a nonzero vacuum rotational transform, ensuring finite confinement even without plasma current. As the plasma current decays to zero, the poloidal vacuum field persists and the ι profile relaxes to ι_{vac} rather than to zero. The decay of the plasma current is described by the external circuit equation (see equation (14)), which was implemented as boundary condition for the current diffusion equation. In the limit of the plasma being a rigid conductor, this equation can be reformulated in terms of the toroidal current using that $U_{\text{pl}} = RI_{\text{tor}} + L_{\text{int}}\mathrm{d}I_{\text{tor}}/\mathrm{d}t$, where R is the electrical resistance of the plasma and L_{int} is the internal inductance:

$$\frac{\mathrm{d}I_{\text{tor}}}{\mathrm{d}t} = -\frac{R}{L}I_{\text{tor}} \tag{36}$$

where L is the total plasma self-inductance defined as $L = L_{\text{int}} + L_{\text{ext}}$. Thus, the evolution of the simulated toroidal current is expected to exhibit an exponential decay to zero.

To determine whether the described behaviour is reflected using ASTRA, a simulation was conducted with an initial toroidal current of 0.4 MA and $U_{\text{ext}} = 0$ V, leading to a decay of the toroidal current. In

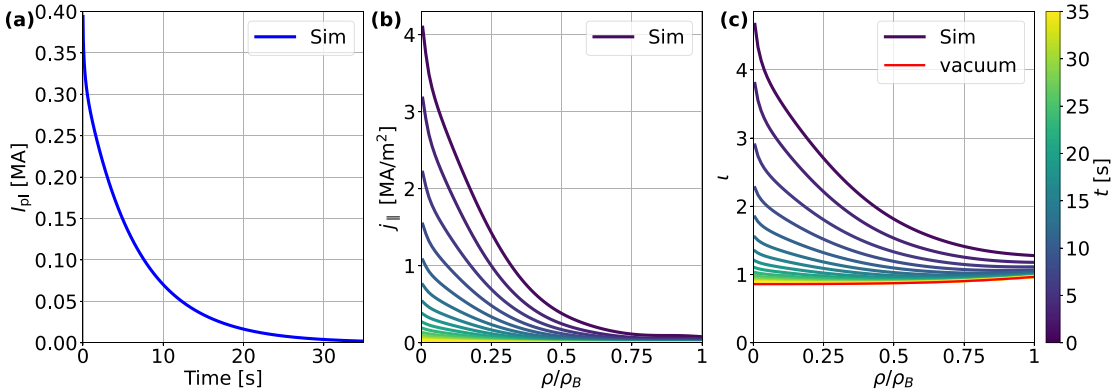

Figure 4. (a) Decay of the simulated total plasma current from initially 0.4 MA. (b) Evolution of the simulated current density to zero. (c) Corresponding ι profile decreases to $\iota_{\mathrm{VMEC}} = \iota_{\mathrm{vac}}$.

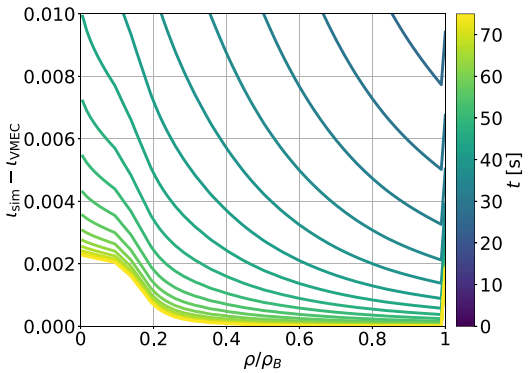

Figure 5. Temporal evolution of the difference between the simulated rotational transform and the profile provided by VMEC.

contrast to the previous simulation, the off-diagonal elements of the susceptance matrix were retained as computed from the VMEC output. As mentioned at the beginning of this section, the employed VMEC equilibrium is the vacuum reference equilibrium of the W7-X discharges 20171206.025 and 20171206.036. Consequently, it does not include a current, and the rotational transform provided by VMEC is the vacuum rotational transform. Contributions from the bootstrap current were neglected in this example case.

The results of this simulation are presented in figure 4. As expected, the total toroidal current decays exponentially, as shown in figure 4(a). Furthermore, figures 4(b) and (c) demonstrate that $j_{||}$ decreases to zero, and ι approaches $\iota_{\mathrm{VMEC}} = \iota_{\mathrm{vac}}$, rather than zero, as would be the case for a tokamak. Figure 5 shows the difference between the simulated ι profile and the one from VMEC. The simulated rotational transform does not match its VMEC counterpart exactly. However, this discrepancy is anticipated and arises from the mismatch in ι_{vac} discussed in the previous section (see figure 1).

This result highlights that, although interpolating the susceptance matrix in the core has only a minimal effect on the susceptance matrix elements themselves (cf figure 2), it is, nevertheless, important for correctly simulating the evolution of ι.

Finally, two test cases from [15] were reproduced. In section 6 of [15], a prescribed Gaussian current distribution and a bootstrap current density computed with NCLASS [40] are used to obtain the steady-state rotational transform for each case. The results are shown in figure 5 of [15]. Note that [15] uses the convention $\zeta = \phi$, which reverses the sign of the rotational transform compared to ASTRA.

In the bootstrap current case in [15], in which the current density vanishes in the core, the rotational transform coincides with the vacuum rotational transform in that region. In contrast, for the prescribed Gaussian current, ι is substantially reduced in the core. This behaviour is consistent with equation (8). Equation (8) also explains the result at the plasma edge: since both current density profiles in [15] produce the same total toroidal current of 161 kA, the toroidal current term in equation (8) is identical for both simulations, resulting in matching values of ι at the edge.

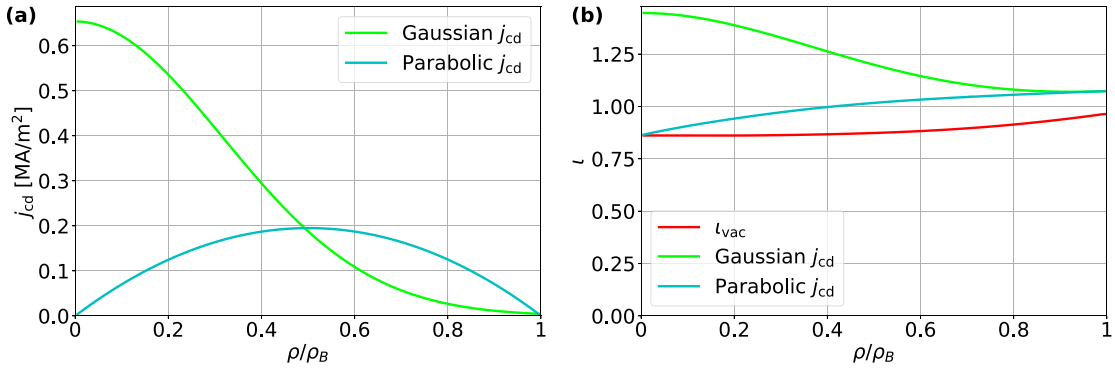

Figure 6. (a) Prescribed current densities used in the final example application of section 4.1. (b) Equilibrated ι profiles corresponding to the current densities in (a) (lime and cyan), compared with the vacuum rotational transform (red).

To compare ASTRA simulations with the results from [15], two scenarios with a prescribed current drive, j_{CD}, were run until the current evolution reached equilibrium, i.e. $j_{\parallel} = j_{CD}$. No other forms of external current drive were included, and the bootstrap current was neglected. Similar current density profiles as in [15] were applied in the presented simulations, using a parabolic profile to mimic the bootstrap current from [15]:

$$j_{\mathrm{CD,par}} = \frac{0.1}{I_{\mathrm{par}}}\left(-\left(\frac{r_{\mathrm{eff}}}{r_{\mathrm{eff,B}}} - 0.5\right)^2 + 0.25\right) \tag{37}$$

$$j_{\mathrm{CD,gau}} = \frac{0.1}{I_{\mathrm{gau}}} \mathrm{e}^{-5(r_{\mathrm{eff}}/r_{\mathrm{eff,B}})^2} \tag{38}$$

where I_{par} and I_{gau} are normalisation factors chosen such that the total driven current for both current density profiles is a prescribed value chosen as 100 kA. The current density profiles are shown in figure 6(a). The corresponding equilibrated ι profiles are presented in figure 6(b), together with the ι_{vac} profile. The profiles qualitatively reproduce the behaviour of the results from [15] discussed above. With the Gaussian current density profile, the rotational transform exceeds the vacuum value in the plasma core, whereas for the parabolic profile with vanishing current density at the magnetic axis, the rotational transform matches ι_{vac} on axis. At the separatrix, the rotational transforms are equal, as both profiles correspond to the same total current (cf equation (8)). A closer agreement with the profiles from [15] could not be expected, as the resulting ι profiles depend on the precise geometry (via the susceptance matrix) and the exact current density profiles employed, which differ between this work and [15].

In the following subsection, the evolution of the current will be validated against experimental results from W7-X.

4.2. Validation against experimental data

In this section, the implementation was benchmarked against W7-X discharges 20171206.025 and 20171206.036. The discharges presented primarily feature electron cyclotron current drive (ECCD) and only a relatively small bootstrap current.

An overview of the time evolution of key plasma parameters during discharge 20171206.025 is presented in figure 7. The heating scenario exclusively employs electron cyclotron resonance heating (ECRH; cf figure 7(a)). Initially, three beams are used to heat the plasma—one core ECRH beam and two obliquely injected beams. After approximately 1.3 s, the core ECRH beam dropped, and only the obliquely injected beams remain for the rest of the discharge. With the reduction in EC heating, the measured diamagnetic energy also decreases (see figure 7(b)). Afterwards, the plasma energy remains approximately constant, displaying a gradual decrease until a significant increase occurs at around 23.6 s due to pellet injection (cf figure 7(b)). Periodic, sawtooth-like crashes of the plasma energy are observed, becoming clearly visible between 5 and 6 s. The core electron temperature, $T_{\mathrm{e,c}}$, measured by ECE (channel 13, at approximately $r/a = 0.05$; see figure 7(c)), rises sharply at the onset of ECRH heating and decreases slightly during the first 0.8 s as the electron density increases (see figure 7(d)). Sawtooth-like crashes in $T_{\mathrm{e,c}}$ are observed from the beginning of the discharge, with the frequency of large crashes (responsible for the sawteeth seen in W_{dia}) decreasing over time. Apart from these sawtooth events, $T_{\mathrm{e,c}}$ remains relatively steady until a sharp drop occurs following pellet injection. A similar behaviour is observed for the measured line-integrated electron density (see figure 7(d)), which increases initially,

is slightly reduced when only two beams remain, and then remains approximately constant until the onset of pellet injection at around 23.6 s, after which it increases rapidly. Experimental Z_{eff} profiles were obtained using bremsstrahlung measurements and Bayesian modelling [37–39]. Figure 7(e) displays the on axis effective charge, $Z_{\mathrm{eff,axis}}$. The total toroidal plasma current, measured using Rogowski coils, is shown in figure 7(f). It should be noted that, in this study, the sign of the current has been reversed relative to previous publications [41, 42], reflecting the definition of the toroidal coordinate used in ASTRA. Following an initial linear increase, the current saturates at approximately 12 kA.

The time interval investigated for this discharge begins with the initiation of ECRH heating at 0 s and concludes at 23 s, shortly before pellets are injected. The time points at which kinetic profiles are specified—between which ASTRA interpolates—were chosen as 0.1 s, 0.85 s, 1.9 s, 4.5 s and 23.0 s. The intervals used to fit the profiles are indicated in figures 7(c) and (d) as vertical transparent lines. The experimental temperature and density profiles at 0.85 s, 1.9 s, 4.5 s and 23.0 s were used to calculate the total ECCD and its main deposition using the ray-tracing code TRAVIS [43]. The Z_{eff} profile required for the TRAVIS calculations was also taken from the experiment. The TRAVIS results were subsequently used to fit Gaussian current drive profiles for the four time points. In the simulations, prior to 0.85 s, the ECCD profile was fixed to the current drive profile at 0.85 s. As noted previously, the bootstrap current played a minor role during the investigated discharges. In the following simulations, the bootstrap current was approximated using a parabolic profile (cf equation (37)) with a total current of 2.5 kA, which is consistent with the estimate from [41]. In an initial approach, the discharge is simulated without a model for the sawtooth crashes.

The result of the simulation is shown in figure 8(a) (blue). The shape of the temporal evolution of I_{tor} closely resembles the experimental observation (black). Rather than exhibiting an immediate increase in toroidal current in response to the driven current, a current opposing the driven current is induced due to Lenz's law (see figure 8(b)). Consequently, the increase in total toroidal current is damped and eventually saturates as I_{tor} approaches the sum of the total bootstrap current and the current driven by ECRH. Nevertheless, the simulated toroidal current rises to a higher value than observed experimentally.

This result is not unexpected, given that sawtooth oscillations have been entirely neglected thus far. As described in previous studies [41, 42], the investigated discharge exhibits two types of crashes: medium-sized crashes, which are visible in the I_{tor} measurement (and, when examining the temperature data, are found to commence immediately following the onset of ECRH rather than only after approximately 5 s), and smaller, more frequent crashes, with several occurring between two medium-sized events. In [42], the medium-sized crashes were attributed to $(m,n) = (1,1)$ modes, while for the high-frequency crashes $(m,n) = (6,5)$ modes were proposed. Crashes are expected to occur when the ι profile exceeds or subceeds $\iota = 1$ and $\iota = 5/6$ sufficiently. Figure 8(d) displays the evolution of the ι profile from the previous simulation during the first 0.4 s. The vacuum rotational transform is illustrated in red, with the two resonances indicated as dotted horizontal lines. Both resonances are crossed shortly after the beginning of the discharge, which is consistent with the occurrence of crashes observed experimentally. As discussed in [42], the repeated sawtooth crashes continuously dissipate magnetic energy. As a consequence, the toroidal plasma current does not reach the sum of ECCD and bootstrap current, but rather saturates at a lower level. This explains why, in the initial simulation, only the shape of the current evolution could be reproduced, while the total current attained higher values than those measured in the experiment.

In the following simulation, a simple Kadomtsev-type model [44], similar to the one described in [42], was implemented. In [42], 1.1 and 0.78 were used as upper and lower limits for the rotational transform at which a crash is triggered. In this work, a minimum sawtooth period of 0.3 s, based on the frequency of medium-sized crashes observed in the experiment, and the condition $\iota > 1$ were imposed as the criteria for reconnection. Consequently, the employed sawtooth model can only account for sawteeth associated with the $\iota = 1$ resonance. The resulting simulation, incorporating the sawtooth model, is shown in figure 8(a) (lime). The total toroidal current reached at the end of the simulated interval is now in good agreement with the experimental data. This confirms the finding from [42] that including sawtooth crashes leads to a reduction in the saturated current. After each crash, both the $j_{\parallel}$ and ι profiles are flattened. However, the peak in the ECCD profile repeatedly drives a peak in the two profiles, thus driving ι above 1 once more and triggering the next crash. This process is visible in figure 8(c), which displays the evolution of the maximum (for $\rho/\rho_{\mathrm{B}} < 0.5$; solid lines) and minimum (dashed lines) values of the ι profile for both simulations. The red dotted lines mark $\iota = 1$ and $\iota = 5/6$. This repeated behaviour explains why the sawtooth crashes persist throughout the discharge. As the minimum of the ι profile repeatedly falls below $\iota = 5/6$, this may also explain the continued occurrence of the smaller crashes. However, as mentioned above, such crashes were not captured by the simple sawtooth model

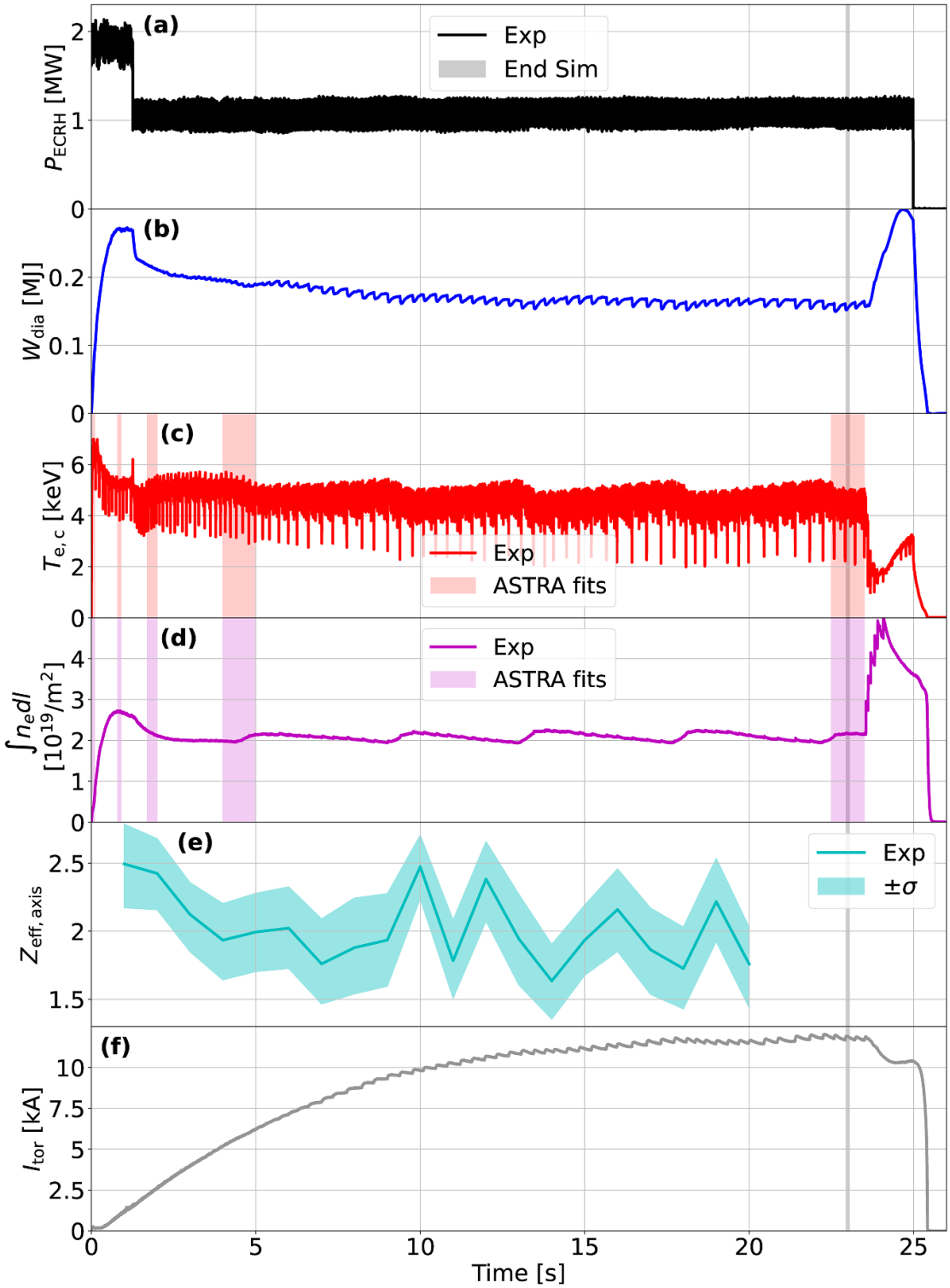

Figure 7. Temporal evolution of experimental measurements from W7-X discharge 20171206.025. The transparent grey line at around 23 s indicates the end of the simulated time interval. (a) ECRH heating power: Note that one beam dropped at around 1.3 s. (b) Measured diamagnetic energy, W_{dia}, throughout the discharge. (c) and (d): Core electron temperature measured at $r/a \approx 0.05$ (c), and line-integrated density (d). Transparent vertical lines at approximately 0.1 s, 0.85 s, 1.9 s, 4.5 s and 23 s denote the intervals for which experimental profiles were fitted for the ASTRA simulations. (e) Experimental effective charge on axis displayed with error bars. (f) Measured total toroidal plasma current.

employed, which was initially designed for tokamaks. Consequently, it is not expected that this simple simulation covers all of the relevant physics and the resulting plasma dynamics. This limitation is also evident in the evolution of the total toroidal current: while relatively large sawteeth are observed experimentally, the simulated I_{tor} displays only much smaller crashes. A more sophisticated sawtooth model

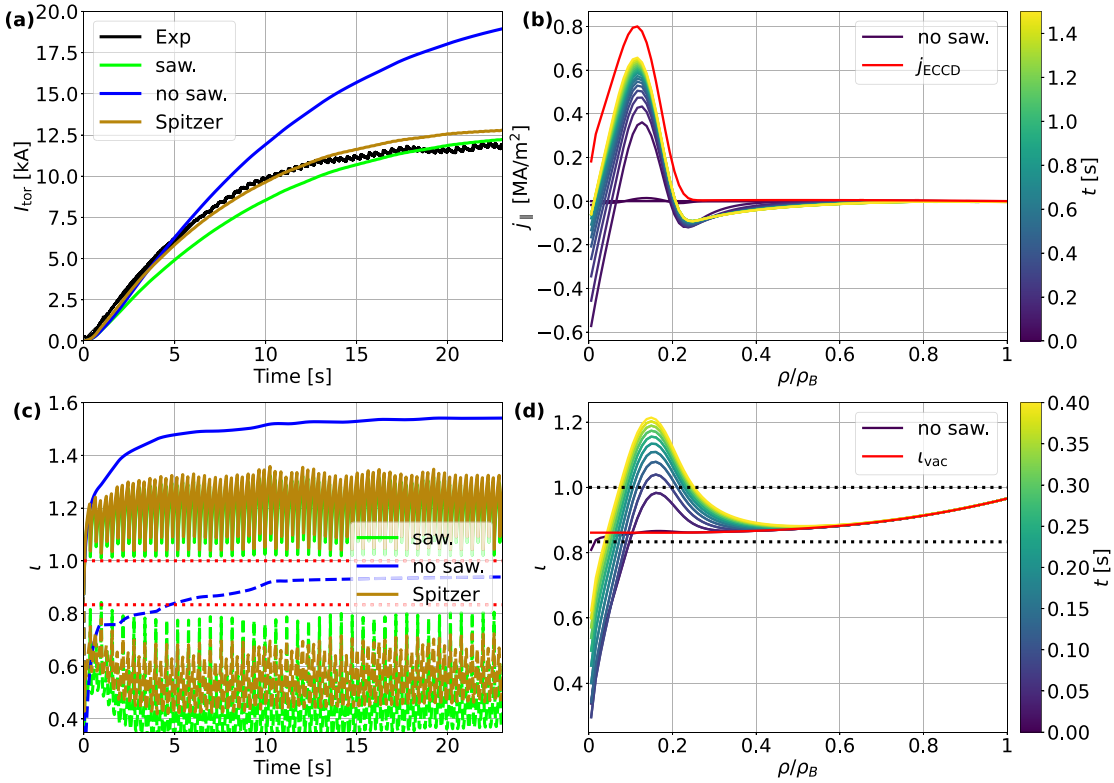

Figure 8. (a) Comparison of the temporal evolution of the toroidal current for discharge 20171206.025. The black line represents the experimental measurement, while the coloured lines correspond to the simulations. The blue line shows the simulation without a sawtooth model, while in the simulation illustrated in lime the Kadomtsev-type sawtooth model was employed. In the brown simulation, the parallel conductivity was estimated using $\sigma_{Sp}(1-f_t)$, where σ_{Sp} denotes Spitzer's conductivity and f_t represents the trapped particle fraction. (b) Evolution of $j_{||}$ profile in the simulation without the sawtooth model (see blue line in subplot (a)) during the first 1.5 s of the discharge. The red profile indicates the j_{ECCD} profile used during the first 0.85 s of the simulated discharge. (c) Evolution of the maximum (for $\rho/\rho_B < 0.5$; solid lines) and minimum (dashed lines) of the ι profile for the simulations of discharge 20171206.025. The red dotted lines mark $\iota = 1$ and $\iota = 5/6$. (d) Evolution of the ι profile in the simulation without the sawtooth model (see blue lines in subplot (c)) during the first 0.4 s of the discharge. The red line indicates ι_{vac}. Again, the dotted lines show $\iota = 1$ and $\iota = 5/6$.

based on Taylor relaxation [45, 46] is currently under development for tokamaks and is expected to provide a more accurate representation of plasma behaviour in future studies.

Although the final total toroidal current at the end of the simulated period matches the measurement when using the presented model, the evolution of the toroidal current still deviates slightly from the experimental data. In the experiment, the current initially increases more rapidly than in the simulation. This discrepancy may be a consequence of the approximated parallel conductivity, which was originally derived for axisymmetric plasmas. A lower conductivity leads to a more rapid decay of the ohmic current opposing the current drive, resulting in a faster increase in the total current.

To illustrate this effect, in a third simulation (see figures 8(a) and (c) in brown), the conductivity was estimated as $\sigma_{Sp}(1-f_t)$, where σ_{Sp} denotes Spitzer's conductivity [47]. The simulated evolution of the toroidal current then closely matches the experimental data over the first 13 s of the discharge. The saturated current at the end of the investigated period is slightly above the experimental value. However, this deviation can readily be explained by uncertainties in the experimental temperature, density, and Z_{eff} profiles, as changes in these profiles significantly affect the amount of current driven by ECCD [48, 49]. Furthermore, the choice of the sawtooth model also influences the saturated current at the end of the simulation.

Despite the remaining discrepancies, it is noteworthy that the simple models chosen for the conductivity and for simulating the sawteeth already result in such good agreement between the simulation and the experiment.

In the remainder of this section, the current diffusion equation is validated against W7-X discharge 20171206.036. An overview of the time evolution of plasma parameters during this discharge is presented in figure 9. In principal, the discharge is similar to the previously investigated discharge

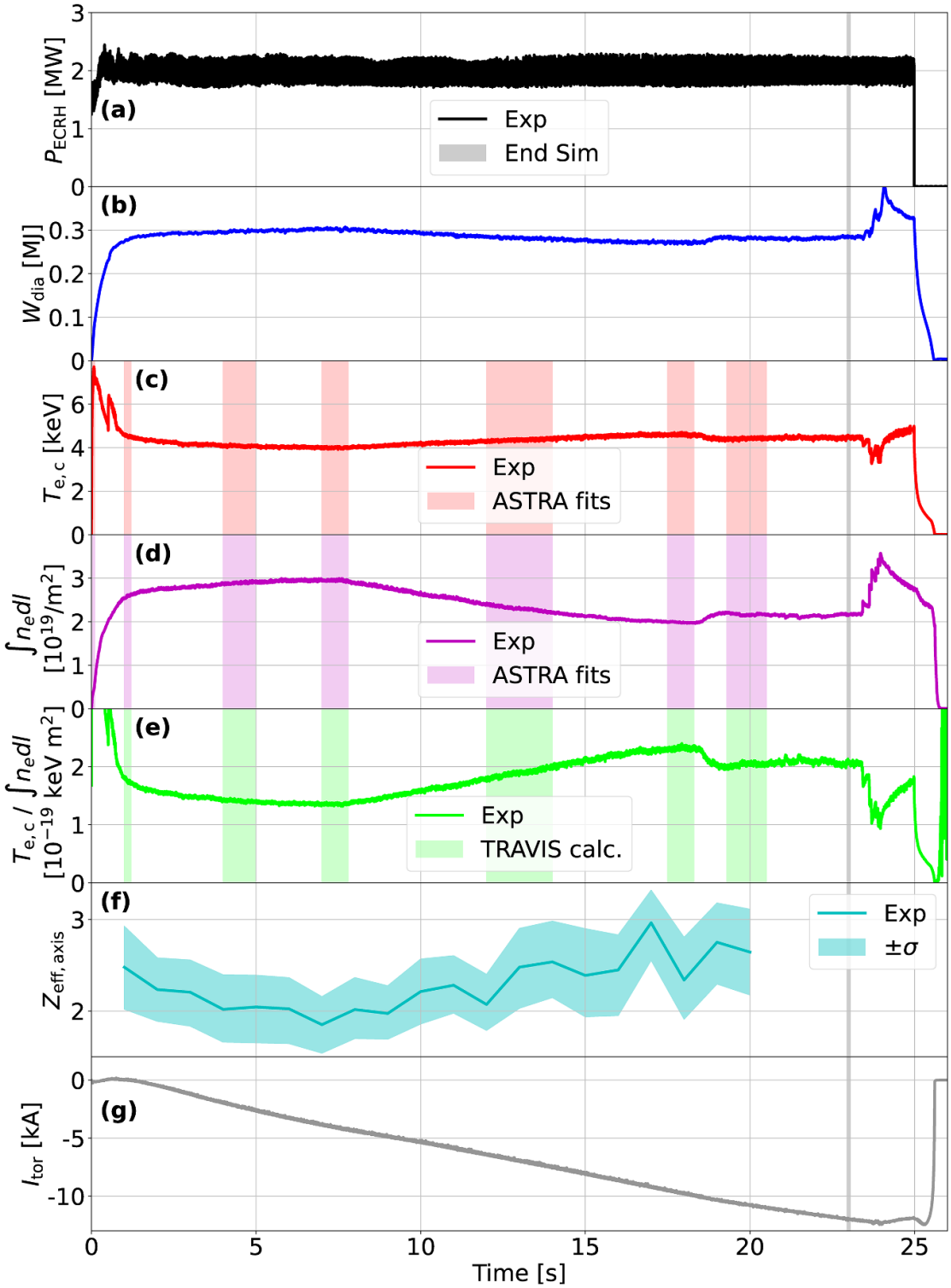

Figure 9. Temporal evolution of experimental measurements from W7-X discharge 20171206.036. The transparent grey line at around 23 s indicates the end of the simulated time interval. (a) ECRH heating power from the experiment. (b) Measured diamagnetic energy, W_{dia}, throughout the discharge. (c) and (d): Core electron temperature measured at $r/a \approx 0.05$ (c), and line-integrated density (d). Transparent vertical lines at around 0.1 s, 1.1 s, 4.5 s, 7.5 s, 13 s, 18 s, and 20 s denote the intervals for which experimental profiles were fitted for the ASTRA simulations. (e) Experimental core electron temperature over line-integrated density as measure for the ECCD efficiency. (f) Experimental effective charge on axis displayed with error bars. (g) Measured total toroidal plasma current.

20171206.025, however, in this case, the direction of the ECCD was reversed (cf figure 9(g)). As a result, instead of increasing ι, the rotational transform is decreased, thereby preventing the occurrence of (1,1) modes. Again, three ECRH beams were used to heat the plasma, combining approximately the same total heating power as at the start of discharge 20171206.025, but this time none of the beams dropped

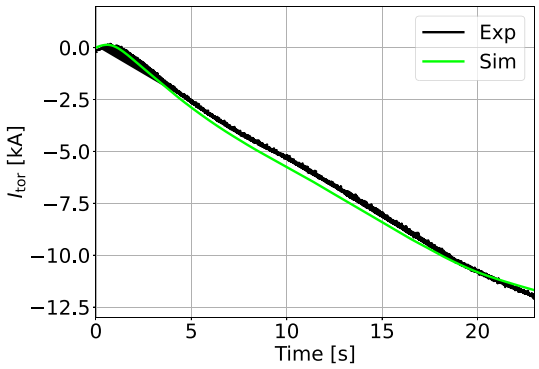

Figure 10. Comparison of the temporal evolution of the toroidal current in discharge 20171206.036. The black line represents the experimental measurement, while the coloured line corresponds to the simulation.

(cf figure 9(a)). In addition, the electron density exhibited much larger variations during discharge 20171206.036 compared to discharge 20171206.025 (see figure 9(d)), which can significantly influence the ECCD efficiency [48, 49]. The changes in the plasma temperature, shown in figure 9(c), also affect the current drive. It was found in [49] that the efficiency of the ECCD scales approximately with T_e/n_e. Figure 9(e) displays the ratio of measured core electron temperature to experimental line-integrated density, which varies during the discharge, significantly affecting ECCD efficiency. To account for the changes in temperature and density, this time, profiles were taken from seven time intervals around 0.1 s, 1.1 s, 4.5 s, 7.5 s, 13 s, 18 s and 20 s (see transparent vertical lines in figures 9(c) and (d)). As before, the simulation covered the first 23 s of the discharge (see grey transparent vertical line in figure 9). After 19.4 s, the kinetic profiles were assumed to remain constant, using the fit obtained from the interval at around 20 s. To account for changes in ECCD efficiency, the ECCD profile was calculated for each interval—except the very early one at 0.1 s—using TRAVIS (see transparent vertical lines in 9(e)), and the same procedure as for the previous discharge. The j_{ECCD} profile was held constant before the first and after the last illustrated interval. The Z_{eff} profile required for the TRAVIS calculations was also taken from the experiment (see figure 9(f)). The expression from [28] was again used to compute the parallel conductivity. As in the previous discharge, the bootstrap current was assumed to have a constant parabolic profile with a total current of 2.5 kA.

The result of this simulation is shown in figure 10(lime) and compared with the experimental evolution of the total toroidal current (black). The simulation is in good agreement with the experimental data. Neglecting the influence of sawteeth in discharge 20171206.025, the evolution of the current is more complex in discharge 20171206.036. Initially, the current is slightly positive. However, after approximately one second, the current reverses direction and remains negative for the duration of the discharge. During this period, the total current increases in an approximately linear fashion. Upon closer inspection, the current begins to saturate slightly as the discharge approaches 10 s, before increasing again more strongly after 10-11 s and then exhibiting further saturation from around 19–20 s. This behaviour is reproduced in the simulation, providing insight into its underlying mechanisms. In the beginning of the discharge, the bootstrap current dominates over the ECRH-driven current, owing to stronger screening of the ECCD, resulting in a net positive current. As the screening effect diminishes, the electron cyclotron driven current becomes dominant, leading to a reversal in the direction of the total current. While the kinetic profiles in 20171206.025 remained relatively constant (when averaged over the sawtooth periods), the kinetic profiles in discharge 20171206.036 change significantly. The combination of a decrease in density and an increase in plasma temperature between approximately 7.8 s and 18.2 s (cf figures 9(c) and (d)) substantially enhances the efficiency of current drive (cf figure 9(e)), and thus gives rise to the observed behaviour of the total plasma current.

Small deviations are visible between the simulated toroidal current and that observed in the experiment. However, these discrepancies are readily accounted for by uncertainties in the calculated ECCD—arising from uncertainties in the employed experimental profiles—and by the use of a conductivity expression derived for axisymmetric plasmas.

In conclusion, it has been demonstrated in this section that, in general, the solutions of the newly implemented generic current diffusion equation are consistent with theoretical expectations. Moreover, the experimental evolution of the toroidal current and rotational transform in a stellarator can now be modelled in ASTRA.

5. Summary and outlook

In this work, a generic current diffusion equation for the poloidal magnetic flux was implemented in the transport solver ASTRA. A coupling to VMEC was also developed, enabling VMEC equilibria to be read and utilised within ASTRA. Finally, the updated current diffusion equation was benchmarked against theoretical expectations and validated against experimental data from W7-X discharges 20171206.025 and 20171206.036.

The implementation in ASTRA of the generic current diffusion equation derived in [15] was described, including the procedure for calculating quantities such as the parallel current density and the rotational transform from the evolution of the poloidal magnetic flux. Furthermore, it was demonstrated that, in the limit of axisymmetric geometry, the generic equation is equivalent to the current diffusion equation used for tokamaks.

Secondly, the unidirectional coupling to VMEC was presented. The susceptance matrix is calculated from the VMEC output file using pySTEL [27]. Subsequently, the matrix elements are transformed into the ASTRA coordinate system and interpolated onto the ASTRA radial grid. Prior to their application in ASTRA, S_{11}, S_{12}, and S_{21} are further subjected to quadratic interpolation in the core to minimise numerical errors.

Lastly, simulations were performed to confirm the correctness and applicability of the current diffusion equation for stellarators. Initially, simple example cases were presented to demonstrate that the implemented equation in ASTRA is consistent with theoretical expectations for a generic current diffusion equation. Subsequently, the equation was validated against the W7-X discharges 20171206.025 and 20171206.036. It was shown that the evolution of the toroidal current in W7-X can be modelled in ASTRA. Moreover, the occurrence of sawteeth-like instabilities observed in the experiment can be related to the ι profile crossing resonant surfaces in the simulation. Employing a simple Kadomtsev-type sawtooth model already led to surprisingly good agreement between the modelled and measured total toroidal current.

In conclusion, ASTRA's underlying transport equations are now valid for both stellarators and tokamaks. As a result, ASTRA is capable of simulating the evolution of the plasma inside the LCFS for both device types, provided that appropriate transport or bootstrap coefficients are supplied as input. In future work, a quasilinear turbulent transport model applicable to stellarators could be developed and implemented in ASTRA to allow for the prediction of particle density and temperature profiles. A dedicated module is already under development to enable the fast calculation of neoclassical transport coefficients, bootstrap current coefficients, the parallel conductivity, and the radial electric field specifically for stellarators. Furthermore, the development of faster 3D equilibrium solvers could motivate the establishment of a bidirectional coupling between ASTRA and such solvers in the future, thereby enabling the incorporation of self-consistent changes of the equilibrium during a discharge. Expanding ASTRA to support stellarators lays the foundation for a stellarator flight simulator and for the predictive modelling of stellarator discharges in the future.

Acknowledgments

This work has been carried out within the framework of the EUROfusion Consortium, funded by the European Union via the Euratom Research and Training Programme (Grant Agreement No 101052200 - EUROfusion). Views and opinions expressed are however those of the author(s) only and do not necessarily reflect those of the European Union or the European Commission. Neither the European Union nor the European Commission can be held responsible for them.

Data availability statement

All data that support the findings of this study are included within the article (and any supplementary files).

ORCID iDs

F Solfronk 0009-0002-9287-1665
E Fable 0000-0001-5019-9685
E Buglione-Ceresa 0009-0009-5360-4530
G Tardini 0009-0002-0544-6880
M Zanini 0000-0002-8717-1106
S Kwak 0000-0001-7874-7575
H Zohm 0000-0002-8870-7806

References

[1] Romanelli M *et al* 2014 *Plasma Fusion Res.* **9** 3403023
[2] Hayashi N JT-60 Team 2010 *Phys. Plasmas* **17** 056112
[3] Fable E *et al* 2022 *Plasma Phys. Control. Fusion* **64** 044002
[4] David P *et al* 2025 *Open Plasma Sci.* **1** 3
[5] Janky F, Fable E, Englberger M and Treutterer W 2021 *Fusion Eng. Des.* **163** 112126
[6] Treutterer W, Fable E, Gräter A, Janky F, Kudlacek O, Gomez Ortiz I, Maceina T, Raupp G, Sieglin B and Zehetbauer T 2019 *Fusion Eng. Des.* **146** A1073–6
[7] Fable E *et al* 2025 *Open Plasma Sci.* **1** 2
[8] Pereverzev G V and Yushma P N 2002 ASTRA. Automated System for Transport Analysis in a Tokamak *IPP Report* Nr. 5-98
[9] Fable E *et al* 2013 *Plasma Phys. Contr. Fusion* **55** 124028
[10] Tardini G *et al* 2026 ASTRA-8: a modern framework for transport analysis and modelling in fusion devices *Plasma Phys. Control. Fusion* submitted
[11] Walker M L, Ambrosino G, De Tommasi G, Humphreys D A, Mattei M, Neu G, Raupp G, Treutterer W and Winter A 2014 *Fusion Eng. Des.* **89** 518–22
[12] di Grazia L E, Fable E, Frattolillo D, Mattei M, David P and Wu C 2023 *Fusion Eng. Des.* **191** 113579
[13] di Grazia L E, Fable E, Mattei M, Siccinio M, Maviglia F and Zohm H 2025 *Fusion Eng. Des.* **215** 114976
[14] Turkin Y, Beidler C D, Maaßberg H, Murakami S, Tribaldos V and Wakasa A 2011 *Phys. Plasmas* **18** 022505
[15] Strand P I and Houlberg W A 2001 *Phys. Plasmas* **8** 2782–92
[16] Strand P I and Houlberg W A 2001 *Fusion Technol.* **39** 1091–5
[17] van Ham L *et al* 2025 *Nucl. Fusion* **65** 036001
[18] Hirshman S P and Whitson J C 1983 *Phys. Fluids* **26** 3553
[19] Hinton F L and Hazeltine R D 1976 *Rev. Mod. Phys.* **48** 239
[20] Helander P *et al* 2012 *Plasma Phys. Control. Fusion* **54** 124009
[21] Gibson A and Taylor J B 1967 *Phys. Fluids* **10** 2653
[22] Xu Y 2016 *Matter Radiat. Extrem.* **1** 192
[23] Bateman G 1973 *Nucl. Fusion* **13** 227
[24] Hirshman S P and Neilson G H 1986 *Phys. Fluids* **29** 790
[25] Ludwig G O and Andrade M C R 1998 *Phys. Plasmas* **5** 2274–83
[26] Schmitt J C 2011 3-D equilibrium reconstruction in the HSX stellarator *PhD Thesis*
[27] Lazerson S *et al* 2020 STELLOPT (Computer software) (https://doi.org/10.11578/dc.20180627.6)
[28] Sauter O, Angioni C and Lin-Liu Y R 1999 *Phys. Plasmas* **6** 2834–9
[29] Taguchi M 1988 *Plasma Phys. Control. Fusion* **30** 1897
[30] Maaßberg H, Beidler C D and Turkin Y 2009 *Phys. Plasmas* **16** 072504
[31] Hirshman S P, Shaing K C, van Rij W I, Beasley C O and Crume E C 1986 *Phys. Fluids* **29** 2951
[32] van Rij W I and Hirshman S P 1989 *Phys. Fluids B* **1** 563
[33] Pasch E, Beurskens M N A, Bozhenkov S A, Fuchert G, Knauer J and Wolf R C 2016 *Rev. Sci. Instrum.* **87** 11E729
[34] Bozhenkov S A *et al* 2017 *J. Instrum.* **12** 10004
[35] Hirsch M *et al* 2019 *EPJ Web Conf.* **203** 03007
[36] Wappl M *et al* 2024 *Rev. Sci. Instrum.* **95** 093529
[37] Svensson J and Werner A 2007 *IEEE Int. Symp. on Intelligent Signal Processing*
[38] Kwak S *et al* 2021 *Rev. Sci. Instrum.* **92** 043505
[39] Pavone A *et al* 2019 *J. Instrum.* **14** C10003
[40] Houlberg W A, Shaing K C, Hirshman S P and Zarnstorff M C 1997 *Phys. Plasmas* **4** 3230
[41] Zanini M *et al* 2020 *Nucl. Fusion* **60** 106021
[42] Aleynikova K *et al* 2021 *Nucl. Fusion* **61** 126040
[43] Marushchenko N B, Turkin Y and Maassberg H 2014 *Comput. Phys. Commun.* **185** 165–76

[44] Kadomtsev B B 1975 *Fiz. Plazmy* **1** 710–5
[45] Taylor J B 1974 *Phys. Rev. Lett.* **33** 1139
[46] Taylor J B 1986 *Rev. Mod. Phys.* **58** 741
[47] Spitzer Jr L and Härm R 1953 *Phys. Rev.* **89** 977
[48] Poli E, Tardini G, Zohm H, Fable E, Farina D, Figini L, Marushchenko N B and Porte L 2013 *Nucl. Fusion* **53** 013011
[49] Luce T C, Lin-Liu Y R, Harvey R W, Giruzzi G, Politzer P A, Rice B W, Lohr J M, Petty C C and Prater R 1999 *Phys. Rev. Lett.* **83** 4550